

Freeze-Casting of Surface-Magnetized Iron(II,III) Oxide Particles in a Uniform Static Magnetic Field Generated by a Helmholtz Coil

Isaac Nelson,* Taylor A. Ogden, Shadi Al Khateeb, Jake Graser, Taylor D. Sparks, Jake J. Abbott, and Steven E. Naleway

Research is conducted into freeze-casting of surface-magnetized Fe_3O_4 particles under uniform, low-strength magnetic fields (5.2 mT) to mimic the mechanical characteristics of natural human bone. Freeze-casting is a technique that fabricates porous materials by directionally freezing and sublimating an aqueous slurry. A novel, Helmholtz coil-based freeze-caster is developed and it is shown that, during freeze-casting, the use of this Helmholtz coil generates a more uniform magnetic field than permanent magnets. This uniform magnetic field, applied in the direction of ice growth, keeps particles from agglomerating and results in an increase of 55% in both the ultimate compressive strength and the elastic modulus of porous surface-magnetized Fe_3O_4 scaffolds. These increases can be linked to a reduction in the porosity that occurs due to magnetic interactions between particles in the presence of the field. These results offer a novel method for the fabrication of bone-inspired biomaterials and structural materials.

1. Introduction

Freeze-casting has been studied for the last 15 years for its promising ability to create controllable porous structures.^[1–3] This process, also referred to as *ice-templating*, requires a fairly inexpensive and maintainable setup. Due to the ability to control the structure, freeze-casting has been proposed to be used for the fabrication of complex composite structures^[3–5] such as synthetic bioceramic bone substitutes,^[6–10] biomimetic structures,^[11,12] dental implants,^[13,14] biodegradable sponges,^[15,16]

cores in sandwiches for structural applications,^[17] and catalyst supports.^[18]

The freeze-casting process requires four steps.^[4,19] First, a slurry is created by mixing a liquid freezing solvent (e.g., water) and solid particles (e.g., ceramic) along with dispersants and polymeric binders (Figure 1a). Second, the slurry is directionally frozen, allowing for the solid particles to segregate and be aligned by the growing ice crystals (Figure 1b). Third, the frozen liquid is sublimated, leaving a porous green scaffold (i.e., non-sintered) that keeps its structure due to the polymeric binder (Figure 1c). Fourth, the green scaffold is sintered, resulting in a porous structure of the rough negative of the grown ice crystals (Figure 1d).

The resultant microstructure of freeze-casting can be controlled in many different ways including altering the particle

size,^[20,21] the percent particle content (in the slurry),^[1] the freezing solvent,^[9,19,22–24] or the freezing direction and rate,^[25] as well as introducing slurry additives,^[26–31] or applying external electric^[32,33] and magnetic fields.^[34–37] Using an external magnetic field can improve the mechanical properties and has been shown to double the ultimate compressive stress (UCS)^[36] and modulus of elasticity (E)^[37] perpendicular to the ice-growth direction (the x -direction as defined in Figure 2) when the magnetic field is applied in this direction. In prior work, applied magnetic fields in the x - and y -directions have been investigated using permanent magnets placed in close proximity to the slurry.^[34–37] However, the use of permanent magnets in the y -direction was shown to create a non-uniform magnetic field distribution that varied between 0 and 500 mT across the sample, thus resulting in particle agglomeration as opposed to pure alignment.^[35]

The use of magnetic particle manipulation, either during freeze-casting or other material fabrication techniques, has been shown to improve mechanical properties by aligning the microstructure.^[35–39] To control particle distribution, the particles need to be responsive to the applied magnetic field. When dealing with certain diamagnetic and paramagnetic materials this can require very high-strength magnetic fields (≈ 1 T),^[39] which can be economically infeasible or physically dangerous. This is because diamagnetic and paramagnetic

I. Nelson, T. A. Ogden, Prof. J. J. Abbott, Prof. S. E. Naleway
Department of Mechanical Engineering
University of Utah
1495 E 100S (1550 MEK), Salt Lake City 84112, UT
E-mail: isaac.d.nelson@utah.edu

J. Graser, Prof. T. D. Sparks
Department of Materials Science & Engineering
University of Utah
122 S Central Campus Dr, #304, Salt Lake City 84112, UT

Dr. S. Al Khateeb
Department of Materials Engineering
Al-Balqa Applied University
Al-Salt, 19117 Jordan

DOI: 10.1002/adem.201801092

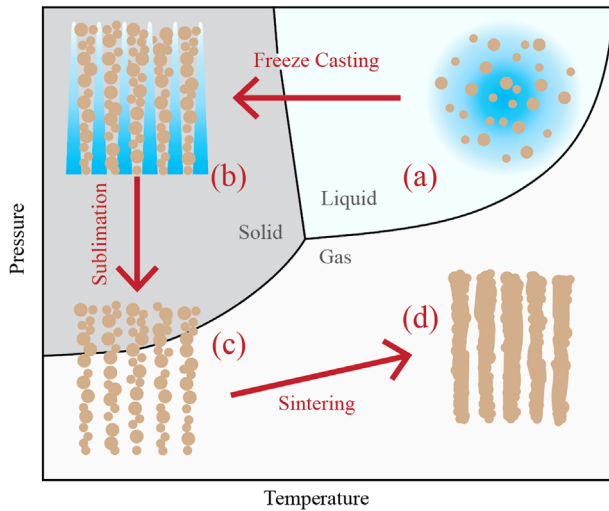


Figure 1. The four-part freeze-casting process on a water temperature-pressure diagram: a) Liquid water is mixed with ceramic particles, polymeric binders, and a dispersant to form an aqueous slurry. b) This slurry is directionally frozen to grow ice crystals and segregate the particles. c) The frozen ice is sublimated, resulting in a green scaffold. d) The green scaffold is sintered, resulting in a ceramic with pores that are the rough negative of the previously grown ice crystals. Figure inspired by refs. [22,65].

materials have low magnetic susceptibility (negative and positive, respectively), making them difficult to use in magnetic applications.^[40] However, superparamagnetic Fe_3O_4 (magnetite) particles can be controlled with low-strength magnetic fields (1–10 mT).^[39] Superparamagnetic particles occur in materials such as Fe_3O_4 when the particle size is so small ($\lesssim 20$ nm) that they can be considered to be a single magnetic domain,^[37,41,42] resulting in magnetic moments for each particle that are in one uniform direction. Superparamagnetic particles are commonly coated with a surfactant and suspended in a carrier fluid (i.e., water) to create a ferrofluid.^[43,44] The unique property of these

particles have been employed through surface magnetization,^[39] where superparamagnetic particles are coated on the surface of larger particles to alter the particles' magnetization. Of particular note, surface magnetization has been employed using an anionic ferrofluid comprised of superparamagnetic Fe_3O_4 particles to manipulate otherwise diamagnetic Al_2O_3 particles.^[37] This surface magnetization process is achieved through an electrostatic interaction between the two oppositely charged particles, which results in a strong bond.^[39]

One tool that has proven useful to manipulate magnetic particles is a Helmholtz coil, which is capable of creating an optimally uniform magnetic field.^[45] A Helmholtz coil is a pair of identical coils connected in series so that they pass the same current, and arranged coaxially such that the distance between the coils is equal to the radius of the coil. Helmholtz coils are used in applications where a highly uniform magnetic field is required, such as to calibrate sensors or to cancel the Earth's magnetic field.^[46] This level of accurate control makes using a Helmholtz coil appealing to manipulate magnetic particles during freeze-casting. Using a uniform magnetic field keeps the particles from agglomerating at the edges of the workspace due to the spatial changes in the field.

In this paper, we investigate the mechanical and structural changes from freeze-casting in the presence of a magnetic field, applied in the direction of ice growth, using surface-magnetized Fe_3O_4 particles. This is done through magnetic particle manipulation using a novel, Helmholtz coil-based freeze-casting setup that, in contrast to previous studies of magnetic freeze-casting that used permanent magnets, will apply an optimally uniform magnetic field. In addition, we aim to use very low-strength magnetic fields to demonstrate the ability of this technique. We propose that using magnetic particle manipulation during freeze-casting will result in the enhancement of the mechanical properties (*UCS* and *E*) by lamellar wall alignment as seen in previous magnetic freeze-casting.^[35–37] We propose that surface magnetization of the ferrimagnetic Fe_3O_4 porous structures, having an even higher magnetic susceptibility is desirable under low-strength magnetic fields.

These results improve our understanding of the effect of controlled magnetic fields on a freeze-cast material's mechanical properties and structure. Specifically, the results will be compared to the properties of natural bone. Because any type of particle can be used during freeze-casting, using biocompatible materials (e.g., hydroxyapatite, fluorapatite) has the potential for applications such as bone replacement. Our results may provide for new advances in biomedical materials that have been made using the freeze-casting process^[6–10] and as anodes for lithium ion batteries.^[47]

2. Experimental Section

2.1. Helmholtz-Coil-Based Magnetic Freeze-Casting Setup

A novel Helmholtz-coil-based freeze-casting setup was fabricated for this research. A custom Helmholtz coil was constructed following the design steps described by Abbott,^[46] as illustrated

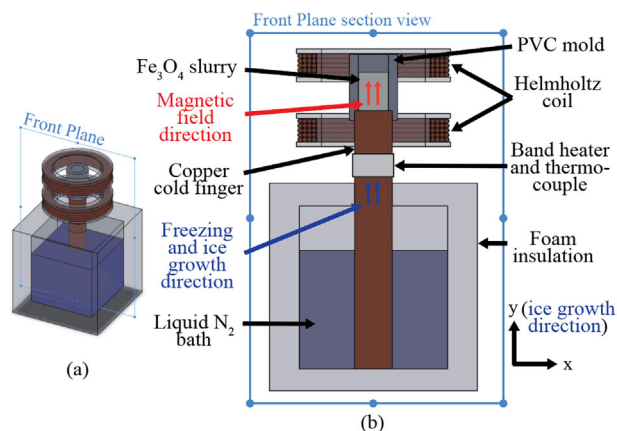


Figure 2. a) An illustrated trimetric view of the freeze-casting setup. b) A front plane section view cut showing the components that make up the magnetic freeze-casting setup, as well as that the magnetic field and freezing direction are aligned in the same direction.

in Figure 2. The Helmholtz coil was centered around the PVC mold, which held the Fe₃O₄ slurry, and set to a height so that the entire Fe₃O₄ slurry was between the coil gap. A uniform magnet field is generated when a current is applied to the Helmholtz coil.^[46] Due to the setup's construction, the ice-growth direction and the magnetic field are parallel to the y-direction. A band heater and thermocouple were connected to a PID controller to control the cooling rate during freeze-casting.

To evaluate how uniform the magnetic field was within the slurry during freezing, measurements were taken using a 3-axis Hall magnetometer with a ±1% accuracy (Metrolab THM1176, Geneva, Switzerland) at points A (center), B (top center), C (top-side edge), and D (side center) of the slurry volume, as shown in Figure 3a. In addition, for cube magnets, which are not radially symmetric, two additional points were analyzed: point E (center back) and point F (top back). At the center of the slurry (point A) there is a symmetry about the y-axis and above and below the x-z-plane so choosing these four points gives a representation of the extreme magnetic field values experienced by the slurry in the Helmholtz coil.

In addition to the magnetic field experimental values, the Biot-Savart Law and Charge Model were used to determine the theoretical uniformity of the magnetic field generated by a Helmholtz coil and permanent magnets (represented by a pair of cube magnets and a ring magnet, two previously explored methods for the manipulation of magnetic particles in freeze-casting), respectively. The Biot-Savart Law can be stated as:

$$\vec{B}(\vec{r}) = \frac{\mu_0}{4\pi} \int_C \frac{I d\vec{\ell} \times \vec{r}'}{|\vec{r}'|^3} \quad (1)$$

where μ_0 is the permeability of free space, C is the path of the current carrying wire, I is the current, $d\vec{\ell}$ is the vector along the wire path C representing a wire element, and \vec{r}' is the vector from the wire element to the point of interest. The Biot-Savart Law was used to describe the magnetic field (\vec{B}) generated by the current carrying wires in the Helmholtz coil (Figure 3a). The Charge Model is used to describe the magnetic field generated by permanent magnets (Figure 3b and c). The Charge Model assumes that the magnetization of the permanent magnet is homogenous and uniform within the magnet so the magnet can be reduced to a "surface charge" on two surfaces,^[48,49] as shown in Figure 3b and c for a ring magnet and cubic magnets, respectively. The magnetic field at a point in space using the Charge Model, \vec{B} , is then given by:

$$\vec{B}(\vec{x}) = \frac{\mu_0}{4\pi} \oint_S \frac{\sigma_m(\vec{x}')(\vec{x} - \vec{x}')}{|\vec{x} - \vec{x}'|^3} dS \quad (2)$$

where $\sigma_m = \vec{M} \cdot \vec{n}$ is the surface charge density, \vec{x}' is the vector from the point of origin to the magnetization vector \vec{M} on the surface of the magnet, \vec{x} is the vector from the origin to the point of interest, and \vec{n} is the surface normal unit vector. Both of these models were used to determine the magnetic field at the same points of interest (points A, B, C, D, E, and F) in the slurry volume as was experimentally measured in the Helmholtz-coil-based freeze-caster. Modeling the magnetic field at points E and F are only necessary in the setup with two permanent cubic magnets because this setup is not radially symmetric.

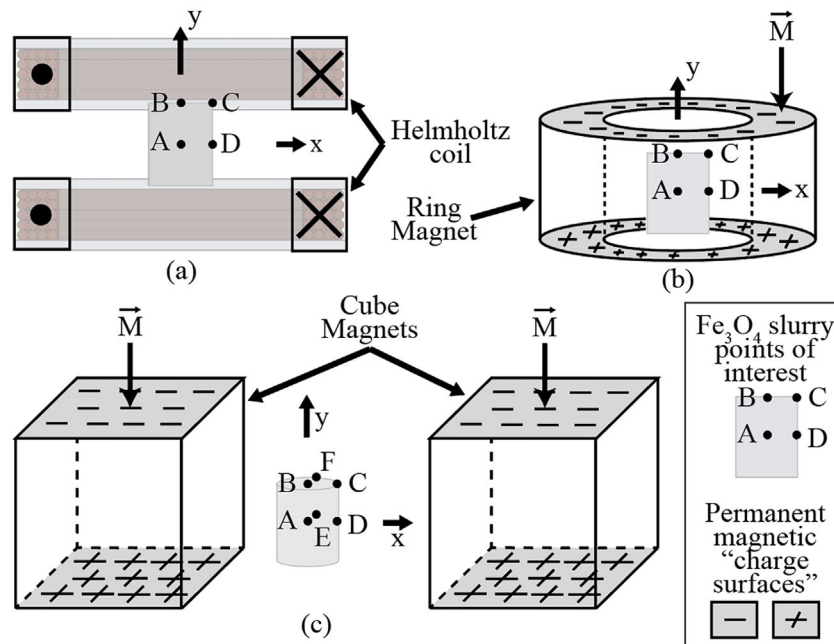


Figure 3. An illustration of the setups used to calculate the magnets fields at points A (center), B (top center), C (top-side edge), and D (side center) in the slurry volume using; a) the Biot-Savart Law and experimentally with a Helmholtz coil, the Charge Model with; b) a ring permanent magnet; and c) two cube permanent magnets which additionally includes points E (center back) and F (top back) because this setup is not radially symmetric. In all cases, the field is in the y-direction at point A.

2.2. Sample Preparation

Ferrimagnetic Fe_3O_4 particles were surface magnetized using procedures similar to those previously established.^[37] First, 47.5 g of ferrimagnetic Fe_3O_4 particles (≈ 250 nm) (ACROS Organics, Pittsburgh, PA, USA) were added to 150 mL of tap water, and separately 1.9 mL of anionic ferrofluid (EMG-705, 3.9 vol% Fe_3O_4 nanoparticles, Ferrotec, Unterensingen, Germany) was added to 75 mL of tap water. The superparamagnetic Fe_3O_4 particles in the ferrofluid have a diameter of ≈ 10 nm. The diluted ferrofluid was then added in 10 mL increments every 1 min to the diluted Fe_3O_4 particles while the solution was being stirred with a glass stirring rod. The mixed solution was tumbled in a ball mill for 24 h followed by boiling off the water on a hot plate. The surface-magnetized Fe_3O_4 particles were then vacuum filtered by being laid in a Buchner funnel on a $0.2\ \mu\text{m}$ pore-size mixed-cellulose-ester filter (Membrane Filters, Fisherbrand, Hampton, NH, USA) and rinsed with tap water to remove the excess surfactant. The particles were then dried at 100°C for 4 h followed by cooling at room temperature. The result of this process was about 47.5 g of surface-magnetized Fe_3O_4 particles.

Aqueous slurries were made with 10 vol% surface-magnetized Fe_3O_4 particles mixed with 1 wt% polyvinyl alcohol of $88\ 000\text{--}97\ 000\ \text{g mol}^{-1}$ (Alfa Aesar, Ward Hill, MA, USA) and 1 wt% polyethylene glycol of $10\ 000\ \text{g mol}^{-1}$ (Alfa Aesar, Ward Hill, MA, USA) as binders, 1 wt% Darvan 811 of $3500\ \text{g mol}^{-1}$ (R. T. Vanderbilt Company, Inc., Norwalk, CT, USA) as a dispersant, and deionized water to create individual slurries that were each 8 mL in volume. These slurries were sealed in a 40 mL plastic bag and mixed by sonicating at 42 kHz for 12 min. Using sonication to mix the slurries is similar to methods that have proven effective in the past reports on freeze-cast slurries.^[50,51] Immediately following mixing, the individual slurries were poured into a PVC freeze-cast mold of diameter 20 mm and then directionally frozen from room temperature at a rate of $10^\circ\text{C min}^{-1}$ within a custom Helmholtz-coil-based magnetic freeze-caster, as illustrated in Figure 2.

Each slurry was prepared the same way to investigate the effects of freezing the slurry while in the presence of different magnetic field strengths. A total of 12 slurries were fabricated and freeze-cast at magnetic field strengths of 0, 2.6, or 5.2 mT with four slurries at each magnetic field strength. The magnetic field was applied constantly in the γ - (i.e., ice growth) direction during the entire freezing process.

Upon being frozen, each slurry was freeze dried at 0.047 mBar and -51°C for 72 h to fully sublimate the ice. Next, the green bodies were sintered in an inert (argon) environment within an alumina tube furnace for 20 min at 1300°C with a heating and cooling rate of $10^\circ\text{C min}^{-1}$, starting and finishing at room temperature. Prior to heating, air was purged from the alumina tube with argon gas followed by flowing argon gas through the tube at $0.5\ \text{L min}^{-1}$ to avoid oxidation of the Fe_3O_4 at 400°C .^[52] The results of this process were porous Fe_3O_4 scaffolds.

2.3. Sample Magnetic Characterization

To determine magnetic susceptibility, magnetization curves were generated using a Microsense FCM-10 vibrating-sample magnetometer (VSM, MicroSense, LLC Lowell, Massachusetts,

USA). This was done to observe how surface magnetizing particles with ferrofluid changes the magnetic properties of the Fe_3O_4 (ferrimagnetic) particles.^[39,40,42,53] Particles (dry Fe_3O_4 , dry surface-magnetized Fe_3O_4 , and as purchased anionic ferrofluid) were subjected to an increasing magnetic field in 10 mT increments between the electromagnets to find the corresponding magnetic moment. The magnetic moment was then divided by the particle mass to get the magnetization in emu g^{-1} .

2.4. Mechanical Characterization

The mid-section of each scaffold was cut into four approximately 4 mm tall half-circle samples (Figure 4) to perform compression tests using an Instron 4303 test frame and 25 kN load cell at a constant crosshead speed of $1\ \text{mm min}^{-1}$. For each scaffold set (0, 2.6, and 5.2 mT), a total of 16 compression tests were performed in the γ -direction to determine the UCS_γ and E_γ . The maximum engineering compression stress that occurred during the test was recorded as the UCS_γ and the slope of the engineering compressive stress to strain in the linear elastic region was recorded as E_γ . All compression samples were in the lamellar structure region and not in the dense structure region. The compression test process was inspired by ASTM standard E9-09.^[54]

2.5. Material Characterization

The microstructure of the scaffolds was determined using a scanning electron microscope (SEM) (FEI Quanta 600 FG, Hillsboro, Oregon, USA). Similarly, the surface-magnetized Fe_3O_4 particles were observed using transmission electron microscopy (TEM) and energy-dispersive X-ray spectroscopy (EDS) to verify the particle sizes and verify that the Fe_3O_4 (≈ 10 nm) from the ferrofluid were adhered to the surface of the larger Fe_3O_4 particles (≈ 250 nm) without additional contamination from the process.

SEM images (5 kV and spot size 3 nm) of each scaffold were taken of the x - z -cross-sections (perpendicular to the mechanical tests, ice growth and magnetic field direction) directly above and below the compression sample surfaces (as noted in Figure 4) to observe the porosity and pore size. This was done to ensure that all the compression test samples were taken above the highly dense region that occurs due to the initial nucleation and rapid growth of the ice crystals and in the region that follows, which is a steady-ice-growth section characterized by lamellar crystal growth, which results in lamellar pores in the final freeze-cast materials.^[19,20] 32 measurements of both the porosity (ratio of pore area to total area) and pore size (μm^2) were performed using Image-J software (Nation Institute of Health, Bethesda, MD, USA) by adjusting the threshold to a value that only allows the dark pores to be present. If a lamellar wall was tilted, the inside of the pore was measured as part of the pore area. Four images of both the upper and lower surfaces for each scaffold were analyzed.

To observe the alignment of the lamellar walls with respect to the direction of applied magnetic field (the γ -direction), SEM

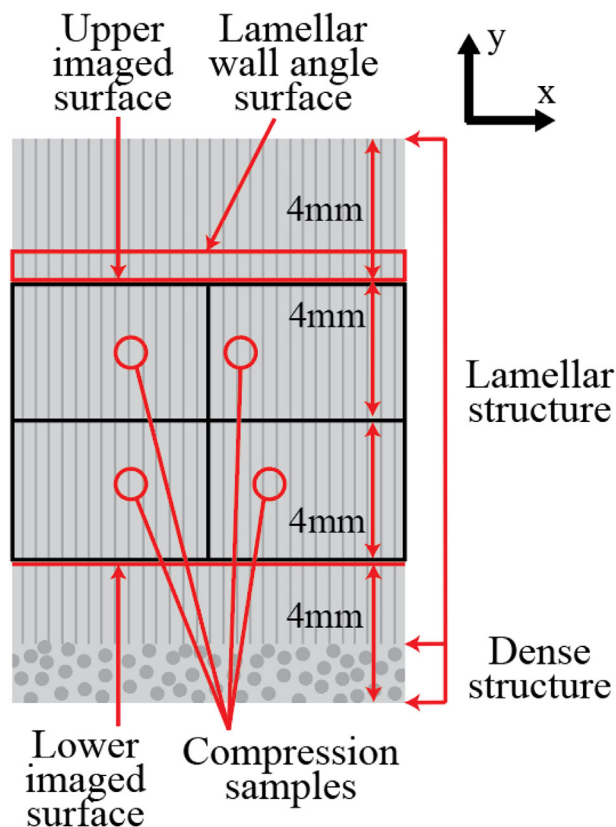


Figure 4. An illustrated cut of a freeze-cast scaffold in the x - y -plane. The compression samples begin from ≈ 4 mm above the bottom of the scaffold. The lower and upper imaged surfaces along with the lamellar wall angle surface are from ≈ 4 mm and ≈ 12 mm above the bottom of the scaffold, respectively. All samples and surfaces analyzed are in the lamellar region of the scaffold above the initial dense region.

images of the x - y -plane-cross-section were taken at the locations shown in Figure 4. Measurements of the angle of the lamellar walls with respect to the y -direction were made using Image-J software (National Institute of Health, Bethesda, MD, USA). Angle measurements were taken on lamellar walls every $\approx 100 \mu\text{m}$ across the diameter of the scaffolds by drawing lines parallel to the walls. A total of 75 measurements were taken for each applied magnetic field (0, 2.6, and 5.2 mT). The lamellar walls at an angle of $\pm 2^\circ$ of the y -direction (i.e., applied magnetic field direction) were said to be aligned with the magnetic field.

2.6. Statistical Analysis

The response variables UCS_y , E_y , porosity, and pore area were each analyzed with respect to the fixed-effect treatment factor *magnetic field strength* using repeated-measures one-way analysis of variance (ANOVA) in MATLAB, with a conventional significance of $\alpha = 0.05$ (two tailed). Three different levels of magnetic field strength were considered: 0, 2.6, and 5.2 mT. If the one-way ANOVA found that there was a significant difference between treatment levels, a Tukey's honest significant difference (HSD) test was performed to determine which levels

were significantly different from each other and which were not. If there was a significant difference found, it is highly likely that the structural and/or mechanical properties were affected by the applied magnetic field. Similar tools have been previously used to statistically analyze freeze-cast scaffolds.^[4] For the UCS_y and E_y , $n = 16$ for each magnetic field strength, for porosity and pore size, $n = 32$ for each magnetic field strength, for lamellar wall alignment, $n = 75$ for each magnetic field strength.

3. Results and Discussion

3.1. Magnetic Freeze-Casting Setup

The Helmholtz-coil-based freeze-casting setup successfully applied a magnetic field throughout the freeze-casting process in the y -direction. The coil produced magnetic fields of 2.6 and 5.2 mT from the application of 1.5 and 3 A, respectively. These current values were chosen because the magnetic field generated would be strong enough for surface-magnetized Fe_3O_4 particles to interact.

The magnetic fields in the slurry volume at points A, B, C, and D found experimentally with the Helmholtz coil and using the Biot-Savart Law to model the Helmholtz Coil (Figure 3a), the Charge Model to model a ring magnet (Figure 3b), and the Charge Model to model two permanent magnets (Figure 3c) are shown in Table 1. The percent error at point B (without loss of generality), relative to a perfectly uniform field, is calculated by:

$$\% \text{ error} = \frac{\|\vec{b}_B - \vec{b}_A\|}{\|\vec{b}_A\|} \cdot 100 \quad (3)$$

where \vec{b}_A is the magnetic field vector in the center of the volume (i.e., the nominal uniform-field value), which for each test is the field at point A (b_{Ax} , b_{Ay}), and \vec{b}_B is the magnetic field vector at point B (b_{Bx} , b_{By}). Vectors at points C, D, E, and F were also compared to the desired point A vector.

Nominal magnetic fields of 2.6 and 120 mT were modeled for each magnetic setup (using Biot-Savart for the Helmholtz coil and the Charge Model for permanent magnets). These were chosen because 2.6 mT is the lowest applied magnetic field in this paper, and 120 mT, as a reference, is a higher magnetic field previously used for freeze-casting.^[36]

In all cases, the point with the highest magnetic field percent error was point C, both experimentally and for the models. This was expected since point C is the farthest from point A, and it has an x -direction magnetic field component that points A, B, D, E, and F do not have.

The NdFeB cube magnets (50.8 mm, grade N42) used in the model were the largest cube magnets available for commercial off-the-shelf purchase (to simulate a setup that could be used in magnetic freeze-casting). To get 2.6 mT at point A, the faces of the cube magnets need to be 394 mm apart (444.6 mm center-to-center). This distance is decreased to 69.4 mm (120.2 mm center-to-center) to get a magnetic field of 120 mT, which is representative of what has been done in previous freeze-cast experiments.^[36] In these calculations, the percent error for

Table 1. Magnetic field values in the slurry volume at points A, B, C, D, E, and F (Figure 3) experimentally measured with the Helmholtz Coil, using the Biot-Savart Law to model a Helmholtz coil (Figure 3a), and the Charge Model to model cube magnets (Figure 3c) and a permanent ring magnet (Figure 3b).

	Direction	A (mT)	B (mT)	C (mT)	D (mT)	E (mT)	F (mT)						
Helmholtz coil	x	0.01	0.01	0.05	0.02								
Experimental	y	2.6	2.58	2.66	2.6								
% Error			0.76	2.78	0.38	radial symm.		A (mT)	B (mT)	C (mT)	D (mT)	E (mT)	F (mT)
Helmholtz coil	x	0	0	0.01	0			0	0	0.43	0		
Model	y	2.6	2.59	2.62	2.60			120	119.4	120.8	119.9		
% Error			0.48	0.78	0.08	radial symm.			0.48	0.78	0.08	radial symm.	
		394 mm apart						69.4 mm apart					
Cube permanent	x	0	0	0.06	0	0	0	0	0	29.34	0	0	0
Magnet model	y	2.6	2.58	2.61	2.63	2.59	2.57	120	110.2	124.3	135.3	116	106.7
	z	0	0	0	0	0	0.02	0	0	0	0	0	7.19
% Error			0.85	2.43	1.26	0.31	1.16		8.14	24.7	12.77	3.32	11.1
		25.4 mm thickness						6.35 mm thickness					
Ring permanent	x	0	0	178.4	0			0	0	65.64	0		
Magnet model	y	356	219.9	332.9	413.0			394.8	35.36	-30.71	394.8		
% Error			38.23	50.53	16.03	radial symm.			91.05	109.1	0.00	radial symm.	

Point A is the nominal magnetic field strength vector of each setup. Modeled 50.8 mm cube magnets are 394 mm and 69.4 mm face-to-face apart, and modeled ring magnets are 25.4 mm ID × 50.8 mm OD × 25.4 mm thickness and 25.4 mm ID × 50.8 mm OD × 6.35 mm thickness.

permanent magnets increases as the magnets are moved closer to the slurry, which is required to increase the magnetic field strength. This increase is found at every point (B, C, D, E, and F) when going from 2.6 to 120 mT at point A.

In order to get two magnetic fields using permanent ring magnets, two off-the-shelf NdFeB magnets (grade N42) with dimensions 25.4 mm ID × 50.8 mm OD × 25.4 mm thickness and 25.4 mm ID × 50.8 mm OD × 6.35 mm thickness were chosen because the slurry diameter can fit within the inner diameter, as shown in Figure 3b. The Charge model shows that using these ring magnets results in a percent error larger than the Helmholtz coil and cube magnets as well as a larger magnetic field at point A. To get low-strength magnetic fields with ring magnets that would fit the slurry volume, a magnet with much lower remanence would need to be used. Custom magnets would likely need to be made to get specific magnetic fields unlike a Helmholtz coil which only requires varying the current to change the magnetic field. In Table 1, it should be noted that the percent error in the Helmholtz coil remains the same as the magnetic field increases because the setup geometry remains constant (i.e., no moving parts).

The experimentally determined Helmholtz coil magnetic fields show a similar trend in percent error compared to the Helmholtz coil model. The percent errors are not the same because in the experimental setup there is an inherent error in the construction of the coil pairs, specifically in making them identical and aligned perfectly coaxial to each other, even though care was taken to minimize these errors during fabrication. In addition, the Hall magnetometer used had an accuracy of ±1%. Experimental errors of this kind would be

present in fabricated permanent-magnet setups as well, thus increasing their error above the modeled results shown in Table 1, especially in setups with moving parts that enable the magnetic field to be adjusted. Regardless, even in this experimental case, the percent error is, on average, lower than those generated by permanent cube magnets and ring magnets at 2.6 mT and considerably lower than those generated by cube magnets at 120 mT (which is representative of a prior magnetic field used in magnetic freeze-casting research^[34–37]). This reduction in percent error enabled our setup to avoid particle agglomeration during freeze-casting.

3.2. Freeze-Cast Scaffolds

Successfully surface-magnetized Fe₃O₄ was observed using TEM and EDS (Figure 5). The surface-magnetized Fe₃O₄ particles have an approximate diameter of 250 nm, with Fe₃O₄ nanoparticles from the ferrofluid approximately 10 nm in diameter visibly contacted to the surfaces of the larger Fe₃O₄. EDS is shown to demonstrate that the only materials present are Fe and O, thus demonstrating that no other contaminants or artifacts of the surface-magnetization process were present in the final surface-magnetized particles. The magnetic susceptibility of the Fe₃O₄ particles was found to remain about the same after surface magnetizing with superparamagnetic Fe₃O₄ particles from the ferrofluid (Figure 6). However, the surface magnetization process enables us to compare our results to prior work.^[37,39]

Increases in the UCS_y and E_y were observed as the applied magnetic field increased, as shown in Figure 7. An increase of 55% in UCS_y and E_y occurs between 0 and 5.2 mT. Additionally,

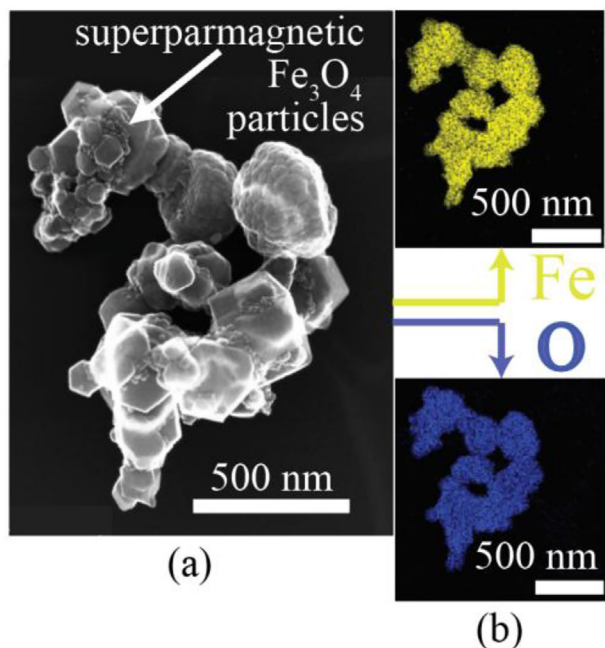


Figure 5. a) A TEM image of surface-magnetized Fe_3O_4 particles (≈ 250 nm) with an arrow indicating a location of several of the smaller superparamagnetic Fe_3O_4 particles (≈ 10 nm). (b) EDS was done to observe that only Fe and O were present on the surface-magnetized Fe_3O_4 .

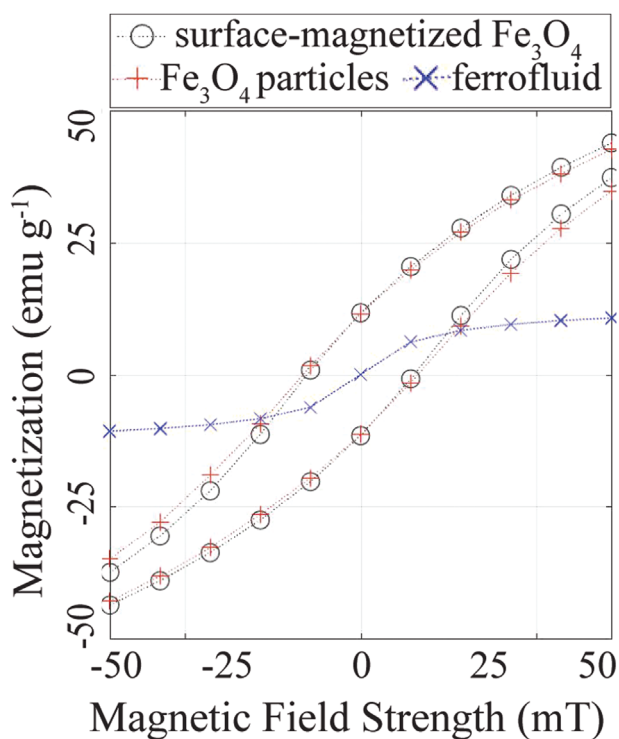


Figure 6. The magnetization curves of surface-magnetized Fe_3O_4 particles, Fe_3O_4 particles (≈ 250 nm), and ferrofluid made with superparamagnetic Fe_3O_4 particles (≈ 10 nm).

an increase of 44% was observed in E_y between 0 and 2.6 mT. As we hypothesized, the interaction of magnetic particles caused by the applied magnetic field creates this increase in UCS_y and E_y . When two Fe_3O_4 particles have magnetic moments \vec{m}_1 and \vec{m}_2 the magnetic dipole interaction energy (E_m) is given by:

$$E_m = -\left(\frac{\mu}{4\pi}\right) \left[\frac{3(\vec{m}_1 \cdot \vec{r})(\vec{m}_2 \cdot \vec{r})}{r^5} - \frac{\vec{m}_1 \cdot \vec{m}_2}{r^3} \right] \quad (4)$$

where μ is the medium permeability, r is the distance between the center of the two particles, and \vec{r} is the vector of the line between the two magnetic dipoles.^[55–57] As the applied magnetic field increases, so do the magnetic moments, resulting in a higher dipole interaction energy between particles. As the interaction energy increases, the particles will come closer to each other and align in the direction of the magnetic field while the ice crystals segregate the particles during ice crystal growth (Figure 1b).

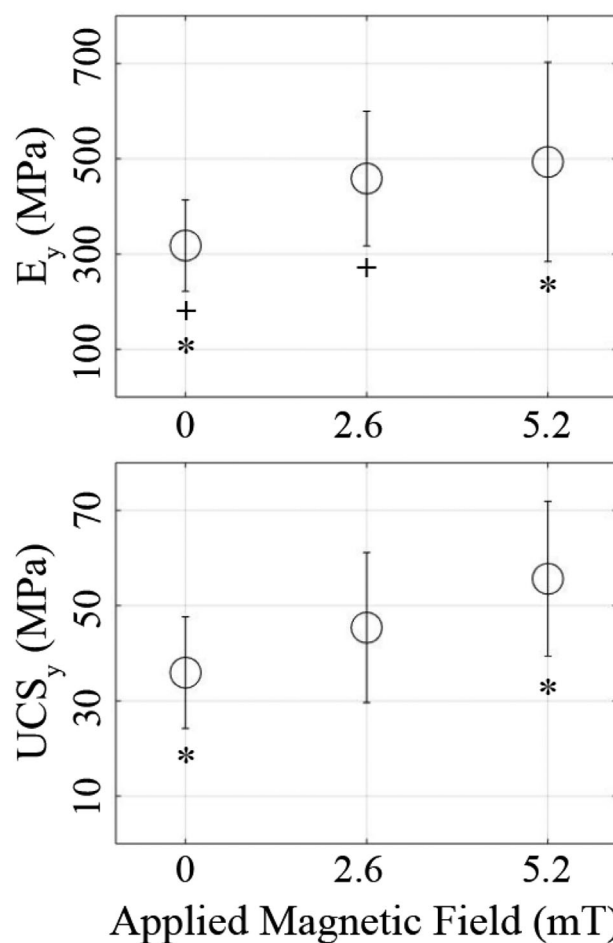


Figure 7. The modulus of elasticity (E_y) and ultimate compressive strength (UCS_y) in the y -direction compared to the constant magnetic field applied to scaffolds during freeze-casting. The values shown are the means \pm one standard deviation. The + and * show pairs of scaffold values that are significantly different ($\alpha = 0.05$).

From Figure 6, we can find the values of the surface-magnetized Fe_3O_4 magnetization (i.e., magnetic moment per gram) \bar{m}_1 and \bar{m}_2 when applying 0, 2.6, and 5.2 mT to be 11.67, 13.95, and 16.25 emu g^{-1} , respectively. Since all the slurries have the same particle content, we can keep the remaining terms (μ , \bar{r} , and r) constant and solve for the percent increase of E_m . Using Equation (4), there is an increase in the magnetic dipole interaction energy of 93% between 0 to 5.2 mT, respectively.

Using the ANOVA test, it was found that there is a significant difference between levels of magnetic field for both the UCS_y and E_y . Using a post-hoc Tukey's HSD test, it was found that significant differences occurs between the 0 and 5.2 mT results for the UCS_y ($p < 0.0005$) and between the 0 and 2.6 mT ($p < 0.0025$) results and the 0 and 5.2 mT ($p < 0.0047$) results for the E_y . Two significantly different levels are indicated using a common symbol in Figure 7.

The mechanical failure of previously reported freeze-cast scaffolds are primarily due to buckling of the lamellar walls.^[28,58–60] Decreasing the pore area can delay lamellar buckling and improve the UCS and E .^[58] As the strength of the applied magnetic field increases, the pore area and porosity decreases and the percent of lamellar walls aligned with the magnetic field increases (Figure 8), which can be connected to the increase in UCS_y and E_y (Figure 9). Scaffold x -cross-section views of each magnetic field are shown in Figure 10a–c, displaying a decrease in the porosity as the magnetic field strength increases. Using ANOVA and Tukey's HSD test, it was found that there is a significant difference between the 0 and 2.6 mT ($p < 0.0055$ for pore size) results and the 0 and 5.2 mT ($p < 0.0003$ for pore size and $p < 0.0075$ for porosity) results. To verify the statistically significant differences observed in the porosity, measurements were taken after infiltrating a scaffold with an epoxy (another technique to measure the structural properties). A statistically significant difference in porosity ($p < 0.0043$) was found between the 0 and 5.2 mT ensuring that the magnetic field did alter the porosity in the x - z -plane. Scaffold x - y -plane views of each magnetic field are shown in Figure 10d–f and show an increase in lamellar wall alignment in the y -direction as the magnetic field strength increases. By using ANOVA and Tukey's HSD test, it was found that there is a significant difference in the measured lamellar wall angles between the scaffolds subject to 0 and 5.2 mT ($p < 0.0039$).

To make sure the pore size and porosity changes are not impacted by the stereological effect, it is important to understand how the tilting of the lamellar walls could affect the outcome of these measurements. Of all the scaffold x - y -plane images, 15.1° was the greatest degree of lamellar wall tilt (from the y -direction) observed and is shown in Figure 10d. Assuming an oval cross-section of the pores and a maximum tilt of 15.1° , a projected cross-section would be reduced by a factor of $\cos(15.1^\circ)$. This would result in a 3.5% difference in the pore area measured in the x -cross-section compared to a pore that was perfectly perpendicular to the x - z -plane. This error does not contribute to changes in the statistically significant differences seen in the pore size and porosity measurements. Additionally, even though there was an observed change in the porosity in the x -cross-section, the volumetric porosity did not change because the same particle content was used.

The compression samples and imaged surfaces were analyzed both above the initial dense region and in the lamellar region (the upper and lower imaged surfaces noted in Figure 4). No statistically significant differences were observed between the

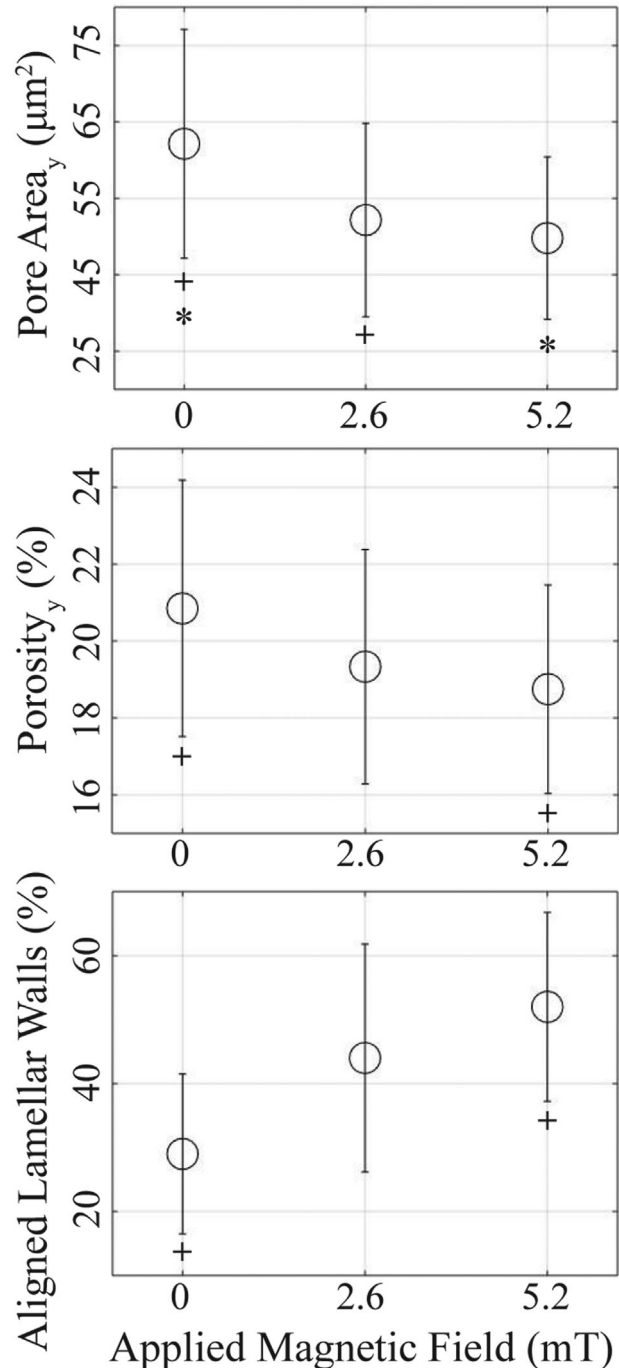


Figure 8. The pore area and porosity in the x -cross-section (normal to y -direction) compared to the constant magnetic field applied to scaffolds during freeze-casting. The values shown are the means \pm one standard deviation. The percentage of lamellar walls aligned with the magnetic field (y -direction) compared to the applied magnetic field. The + and * show pairs of scaffold values that are significantly different ($\alpha = 0.05$).

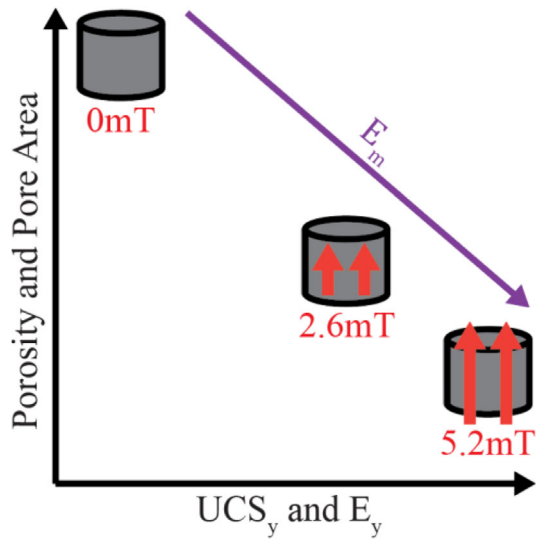


Figure 9. A graphic illustration of the how applying a magnetic field during freeze-casting changes the mechanical (UCS_y and E_y), structural (porosity and pore area) and magnetic dipole interaction energy (E_m) of a scaffold. The increase in mechanical properties and decrease in pore area and porosity are proportional to the magnetic dipole interaction energy.

two locations using ANOVA. Therefore, no indication was found of significant particle agglomeration, which would cause the properties to change spatially throughout the scaffolds. This is likely due to the uniformity of the magnetic field generated from the Helmholtz coil.

3.3. Comparison to Previous Results

Previous experiments have shown an increase in the mechanical properties in the x -direction with a setup of an applied magnetic field in the x -direction and freezing in the y -direction. 100% increases in UCS_x and E_x were observed between 0 and 120 mT with surface-magnetized TiO_2 ,^[36] and a 100% increase in E_x was observed between 0 and 75 mT with surface-magnetized Al_2O_3 .^[37] Because of the non-uniformity that occurs using permanent magnets, the previous experiments had not had success with improving the y -direction mechanical properties. Particle agglomeration occurred because of the magnetic field gradient that ring permanent magnets produce when trying to apply a y -direction magnetic field.^[35] This particle agglomeration did not occur in our scaffolds, as demonstrated by the fact that the mechanical and structural properties did not deviate throughout the lamellar region. By using a Helmholtz coil it was possible to create a highly uniform magnetic field oriented in the y -direction, which resulted in an increase in the UCS_y and E_y of 55% between applying 0 and 5.2 mT. Therefore, by using materials with a higher magnetic susceptibility and a more uniform field, the current work was able to provide over half of the increase in mechanical properties with magnetic manipulation while applying a magnetic field that was less than 10% strength compared to prior work. This suggests that increasing the magnetic field beyond 5.2 mT has the potential to increase the y -direction mechanical properties even further.

While Fe_3O_4 is not a commonly applied biomedical material, freeze-casting with biocompatible ceramics such as hydroxyapatite has shown potential for biomedical applications^[7–9] and the current techniques of surface magnetization and magnetic

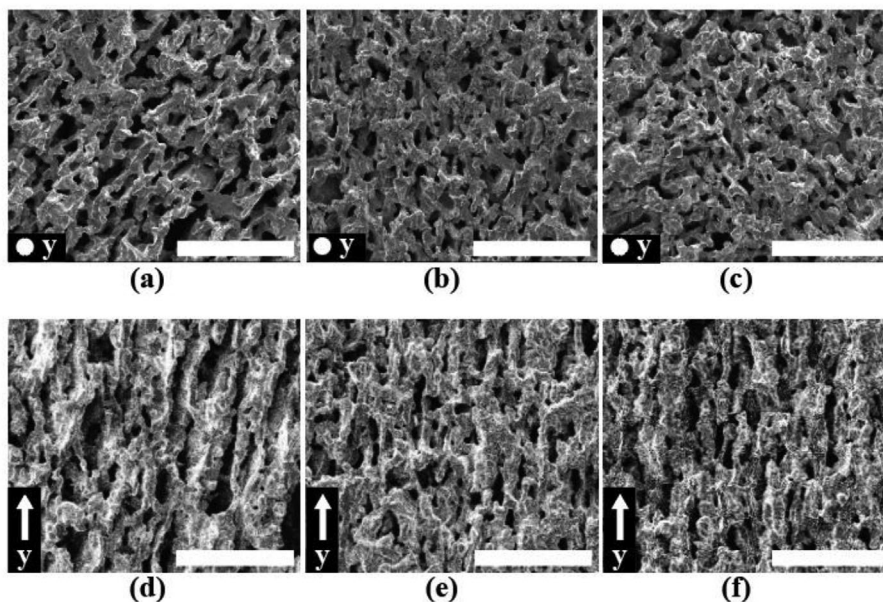


Figure 10. An SEM imaged surface of; a) 0 mT, b) 2.6 mT, and c) 5.2 mT scaffold used to measure the porosity and pore size in the x -cross-section. The mean pore size was $62.1 \mu m^2$, $52.2 \mu m^2$, and $49.8 \mu m^2$ and the mean porosity was 20.8%, 19.3%, and 18.7% for the 0 mT, 2.6 mT, and 5.2 mT scaffolds, respectively. An SEM imaged surface of; d) 0 mT, e) 2.6 mT, and f) 5.2 mT scaffold used to measure the percent of walls aligned with the magnetic field direction (y -direction). The greatest degree of lamellar wall tilt observed was 15.1° in (d). All the scale bars are $100 \mu m$.

freeze-casting with a Helmholtz-coil-based setup could be easily applied to these materials. The structure of freeze-cast materials is able to mimic the complex porosity of bone (both cancellous and cortical), thus allowing for these structures to promote osteoblast cell growth.^[61] The mechanical characteristics of bone vary greatly depending on factors such as the location, type, age, a person's activity level, and history. However, typically the UCS, E, and porosity for cancellous bone are 1.5–5 MPa, 100–500 MPa, and 75–95%, respectively, and for cortical bone are 195 MPa, 17.4 GPa, and 5–10%, respectively.^[62] The fabricated surface-magnetized Fe₃O₄ scaffolds are within the mechanical and structural properties of both cancellous and cortical bone, suggesting that these techniques may enable the development of novel biomedical implants that mimic both the structure and mechanical properties of natural bone. Mimicking the properties of bone will enable these implants to reduce stress shielding that occurs with implants that are considerably stronger than natural bone.^[63,64]

4. Conclusions

The current study of freeze-casting of surface-magnetized Fe₃O₄ with the application of a unidirectional magnetic field via a Helmholtz coil enables the following conclusions:

- 1) A Helmholtz coil (modeled using the Biot-Savart Law) has a more uniform magnetic field (< 1% error) than equivalent-strength permanent magnets (modeled using the Charge Model). With a custom built Helmholtz coil, the uniform magnetic field did not agglomerate surface-magnetized Fe₃O₄ particles during the application of low-strength magnetic fields of 2.6 and 5.2 mT.
- 2) The mechanical properties, UCS_y and E_y, of freeze-cast surface-magnetized Fe₃O₄ scaffolds were increased by 55% by applying a 5.2 mT magnetic field during freezing, when compared to no application of magnetic field (0 mT).
- 3) The scaffold structural properties, pore area and porosity, decreased by 20% and 10%, respectively, by applying a 5.2 mT magnetic field when compared to no application of magnetic field (0 mT).
- 4) The percent of lamellar walls aligned with the magnetic field increased from 29% to 52% by applying a 5.2 mT magnetic field when compared to no application of magnetic field (0 mT).
- 5) The application of a magnetic field increases the magnetic dipole interaction energy, making it more energetically favorable for the surface-magnetized Fe₃O₄ particles to align, resulting in the higher mechanical properties and lower porosities observed.

Acknowledgements

This work was financially supported in part by the National Science Foundation under grant CMMI #1660979. The authors thank Matt Cavilla of the University of Utah Telerobotics lab for his suggestions on winding a Helmholtz coil, Ali Borjali of the University of Utah Tribology and Precision Engineering lab for helpful discussions on current controllers,

and Advanced Motion Control for generous academic discounts on the servo drives used to control the Helmholtz coil.

The manuscript has been modified after online publication.

Conflict of Interest

The authors declare no conflict of interest.

Keywords

bioinspired, freeze-casting, Helmholtz coil, porous material, surface-magnetized Fe₃O₄

Received: October 15, 2018

Revised: December 7, 2018

Published online: January 16, 2019

- [1] S. W. Sofie, F. Dogan, *J. Am. Ceram. Soc.* **2001**, *84*, 1459.
- [2] K. Araki, J. W. Halloran, *J. Am. Ceram. Soc.* **2005**, *88*, 1108.
- [3] S. Deville, E. Saiz, R. K. Nalla, A. P. Tomsia, *Science* **2006**, *311*, 8.
- [4] S. E. Naleway, K. C. Fickas, Y. N. Maker, M. A. Meyers, J. McKittrick, *Mater. Sci. Eng. C* **2016**, *61*, 105.
- [5] M. E. Launey, E. Munch, D. H. Alsem, E. Saiz, A. P. Tomsia, R. O. Ritchie, *J. R. Soc. Interface* **2010**, *7*, 741.
- [6] H. Yoshikawa, A. Myoui, *J. Artif. Organs* **2005**, *8*, 131.
- [7] S. Deville, E. Saiz, A. P. Tomsia, *Biomaterials* **2006**, *27*, 5480.
- [8] Y. Tang, K. Zhao, L. Hu, Z. Wu, *Ceram. Int.* **2013**, *39*, 9703.
- [9] E.-J. Lee, Y.-H. Koh, B.-H. Yoon, H.-E. Kim, H.-W. Kim, *Mater. Lett.* **2007**, *61*, 2270.
- [10] G. Wei, P. X. Ma, *Biomaterials* **2004**, *25*, 4749.
- [11] L. B. Mao, H. L. Gao, H. B. Yao, L. Liu, H. Colfen, G. Liu, S. M. Chen, S. K. Li, Y. X. Yan, Y. Y. Liu, S. H. Yu, *Science* **2016**, *354*, 107.
- [12] E. Munch, M. E. Launey, D. H. Alsem, E. Saiz, A. P. Tomsia, R. O. Ritchie, *Science* **2008**, *322*, 20.
- [13] H.-D. Jung, S.-W. Yook, H.-E. Kim, Y.-H. Koh, *Mater. Lett.* **2009**, *63*, 1545.
- [14] H. D. Jung, S. W. Yook, T. S. Jang, Y. Li, H. E. Kim, Y. H. Koh, *Mater. Sci. Eng. C* **2013**, *33*, 59.
- [15] H. W. Kang, Y. Tabata, Y. Ikada, *Biomaterials* **1999**, *20*, 1339.
- [16] H. Schoof, J. Apel, I. Heschel, G. Rau, *J. Biomed. Mater. Res.* **2001**, *58*, 352.
- [17] Y. Chino, D. C. Dunand, *Acta Mater.* **2008**, *56*, 105.
- [18] L. Ren, Y.-P. Zeng, D. Jiang, *Ceram. Int.* **2009**, *35*, 1267.
- [19] S. Deville, *J. Mater. Res.* **2013**, *28*, 2202.
- [20] S. Deville, E. Maire, A. Lasalle, A. Bogner, C. Gauthier, J. Leloup, C. Guizard, *J. Am. Ceram. Soc.* **2010**, *93*, 2507.
- [21] G. Liu, T. W. Button, *Ceram. Int.* **2013**, *39*, 8507.
- [22] S. Deville, *Adv. Eng. Mater.* **2008**, *10*, 155.
- [23] R. Liu, T. Xu, C.-A. Wang, *Ceram. Int.* **2016**, *42*, 2907.
- [24] M. C. Gutierrez, M. L. Ferrer, F. del Monte, *Chem. Mater.* **2008**, *20*, 48.
- [25] W. L. Li, K. Lu, J. Y. Walz, *Int. Mater. Rev.* **2013**, *57*, 37.
- [26] E. Munch, E. Saiz, A. P. Tomsia, S. Deville, *J. Am. Ceram. Soc.* **2009**, *92*, 1534.
- [27] S. E. Naleway, C. F. Yu, M. M. Porter, A. Sengupta, P. M. Iovine, M. A. Meyers, J. McKittrick, *Mater. Des.* **2015**, *71*, 62.
- [28] S. E. Naleway, C. F. Yu, R. L. Hsiong, A. Sengupta, P. M. Iovine, J. A. Hildebrand, M. A. Meyers, J. McKittrick, *Acta Mater.* **2016**, *114*, 67.
- [29] M. Fukushima, Y.-I. Yoshizawa, T. Ohji, *Adv. Eng. Mater.* **2014**, *16*, 607.

- [30] Y. Zhang, K. Zuo, Y.-P. Zeng, *Ceram. Int.* **2009**, *35*, 2151.
- [31] J. Zeng, Y. Zhang, K.-C. Zhou, D. Zhang, *Trans. Nonferrous Met. Soc. China* **2014**, *24*, 718.
- [32] Y. Zhang, L. Hu, J. Han, *J. Am. Ceram. Soc.* **2009**, *92*, 1874.
- [33] Y. Tang, S. Qiu, Q. Miao, C. Wu, *J. Eur. Ceram. Soc.* **2016**, *36*, 1233.
- [34] M. M. Porter, L. Meraz, A. Calderon, H. Choi, A. Chouhan, L. Wang, M. A. Meyers, J. McKittrick, *Compos. Struct.* **2015**, *119*, 174.
- [35] M. M. Porter, P. Niksiar, J. McKittrick, G. Franks, *J. Am. Ceram. Soc.* **2016**, *99*, 1917.
- [36] M. M. Porter, M. Yeh, J. Strawson, T. Goehring, S. Lujan, P. Siripasopsotorn, M. A. Meyers, J. McKittrick, *Mater. Sci. Eng. A* **2012**, *556*, 741.
- [37] M. B. Frank, S. E. Naleway, T. Haroush, C.-H. Liu, S. H. Siu, J. Ng, I. Torres, A. Ismail, K. Karandikar, M. M. Porter, O. A. Graeve, J. McKittrick, *Mater. Sci. Eng. C* **2017**, *77*, 484.
- [38] M. M. Porter, *Bioinspired Design: Magnetic Freeze Casting*, UC San Diego, **2014**. <https://escholarship.org/uc/item/39z9x080>
- [39] R. M. Erb, R. Libanori, N. Rothfuchs, A. R. Studart, *Science* **2012**, *335*, 199.
- [40] C. Carter, M. Norton, *Ceramic Materials*, Springer, New York, NY, USA **2013**, p. 766.
- [41] D. K. Kim, Y. Zhang, W. Voit, K. V. Rao, M. Muhammed, *J. Magn. Magn. Mater.* **2001**, *225*, 30.
- [42] D. Jiles, *Introduction to Magnetism and Magnetic Materials*, 3rd ed.; Chapman & Hall, New York, NY, USA **1998**.
- [43] M. Marolt, Z. Jaglicic, *Superparamagnetic Materials*, University of Ljubljana, Kranj **2014**.
- [44] E. V. Groman, L. Josephson, J. M. Lewis, Biologically degradable superparamagnetic materials for use in clinical applications, US Patent at Alexandria, VA, USA **1989**.
- [45] A. W. Mahoney, J. C. Sarrazin, E. Bamberg, J. J. Abbott, *Adv. Rob.* **2011**, *25*, 1007.
- [46] J. Abbott, *Rev. Sci. Instrum.* **2015**, *86*, 10.
- [47] Y. Chen, H. Xia, L. Lu, J. Xue, *J. Mater. Chem.* **2012**, *22*, 5006.
- [48] J. L. G. Janssen, *Extended Analytical Charge Modeling for Permanent-Magnet Based Devices: Practical Application to the Interactions in a Vibration Isolation System*, Technische Universiteit Eindhoven, Eindhoven **2011**.
- [49] M. F. J. Kremers, J. J. H. Paulides, E. Ilhan, J. L. G. Janssen, E. A. Lomonova, *IEEE Trans. Magn.* **2013**, *49*, 2299.
- [50] A. M. A. Silva, E. H. M. Nunes, D. F. Souza, D. L. Martens, J. C. Diniz da Costa, M. Houmard, W. L. Vasconcelos, *Ceram. Int.* **2015**, *41*, 10467.
- [51] D. F. Souza, E. H. M. Nunes, D. S. Pimenta, D. C. L. Vasconcelos, J. F. Nascimento, W. Grava, M. Houmard, W. L. Vasconcelos, *Mater. Character.* **2014**, *96*, 183.
- [52] T. K. Sandeep Kumar, *Investigation of Sintering Kinetics of Magnetite Pellets During Induration*, Luleå University of Technology, Luleå, Sweden **2015**.
- [53] A. Guimaraes, *Principles of Nanomagnetism*, Springer, New York, NY, USA **2009**.
- [54] ASTM Standard E9-09: Standard Test Methods of Compression Testing of Metallic Materials at Room Temperature, ASTM International, West Conshohocken, PA, USA, **2012**, <https://doi.org/10.1520/e0009-09>, <http://www.astm.org>
- [55] S. Tokura, M. Hara, N. Kawaguchi, N. Amemiya, *J. Magn. Magn. Mater.* **2016**, *411*, 68.
- [56] J. G. Ku, X. Y. Liu, H. H. Chen, R. D. Deng, Q. X. Yan, *AIP Adv.* **2016**, *6*, 025004.
- [57] M. Cacciola, A. Berdie, *Acta Phys. Pol., A* **2016**, *129*, 88.
- [58] M. M. Porter, R. Imperio, M. Wen, M. A. Meyers, J. McKittrick, *Adv. Funct. Mater.* **2014**, *24*, 1978.
- [59] A. Lichtner, D. Roussel, D. Jauffres, C. L. Martin, R. K. Bordia, *J. Am. Ceram. Soc.* **2016**, *99*, 979.
- [60] J. Seuba, S. Deville, C. Guizard, A. J. Stevenson, *Sci. Rep.* **2016**, *6*, 24326.
- [61] H. Bai, D. Wang, B. Delattre, W. Gao, J. De Coninck, S. Li, A. P. Tomsia, *Acta Biomater.* **2015**, *20*, 113.
- [62] R. B. Martin, D. B. Burr, N. A. Sharkey, D. P. Fyhrie, *Skeletal Tissue Mechanics*, Vol. 2nd, Springer-Verlag, New York **2015**.
- [63] S. Shadanbaz, G. J. Dias, *Acta Biomater.* **2012**, *8*, 20.
- [64] G. Ryan, A. Pandit, D. P. Apatsidis, *Biomater.* **2006**, *27*, 2651.
- [65] M. M. Porter, J. McKittrick, M. A. Meyers, *JOM* **2013**, *65*, 720.